

## BAYESIAN FUNCTIONAL REGISTRATION OF FMRI DATA

BY GUOQING WANG, ABHIRUP DATTA AND MARTIN A. LINDQUIST

*Department of Biostatistics, Johns Hopkins University, [mlindqui@jhu.edu](mailto:mlindqui@jhu.edu)*

Functional magnetic resonance imaging (fMRI) has provided invaluable insight into our understanding of human behavior. However, large inter-individual differences in both brain anatomy and functional localization after anatomical alignment remain a major limitation in conducting group analyses and performing population level inference. This paper addresses this problem by developing and validating a new computational technique for reducing misalignment across individuals in functional brain systems by spatially transforming each subjects functional data to a common reference map. Our proposed Bayesian functional registration approach allows us to assess differences in brain function across subjects and individual differences in activation topology. It combines intensity-based and feature-based information into an integrated framework, and allows inference to be performed on the transformation via the posterior samples. We evaluate the method in a simulation study and apply it to data from a study of thermal pain. We find that the proposed approach provides increased sensitivity for group-level inference.

**1. Introduction.** In recent years functional magnetic resonance imaging (fMRI) has provided invaluable insight into understanding the neurophysiological underpinnings of human behavior. Much of these gains have been driven by the combination of increasingly sophisticated statistical and computational techniques and the ability to capture brain data at finer spatial and temporal resolution. Together, these advances are allowing researchers to study brain-behavior correlations and develop population-level models of the functional brain representations underlying behavior, performance, clinical status and prognosis. However, a fundamental obstacle to using emerging analytic techniques effectively in these settings is individual variation in functional brain anatomy. That is, the fact that the precise locations of brain activation are not perfectly aligned across subjects. Addressing this obstacle will greatly extend the capability to perform group-level hypothesis testing, use machine learning to develop population-level brain models that predict behavior, and take advantage of the full spatial resolution of fMRI.

In a task-based fMRI study, each subject is typically administered one or more stimuli and observed at hundreds of time points. At each time point, the subject's blood oxygenation level dependent (BOLD) response is recorded at roughly 100,000 spatial locations (voxels), giving rise to multivariate time series data. In order to properly perform statistical analysis over multiple subjects, it is necessary for each voxel to lie within the same brain structure for each subject. This does not occur naturally, as all subjects have brains of different sizes and shapes. Therefore, to achieve this goal all subjects' brains are normalized to a stereotaxic space prior to analysis.

Typically, normalization is performed using a high-resolution anatomical scan that is acquired in the same session and spatially aligned with the fMRI data. Current standard practice is to use nonlinear transformations to warp individual subjects' anatomical scan to an average, anatomically based 3D reference space (e.g., the "Montreal Neurologic Institute" (MNI) space). These transformations are then applied to the fMRI data to ensure they lie in MNI space, and data can be compared across subjects (Lindquist et al., 2008; Ombao et al., 2016).

---

*Keywords and phrases:* functional magnetic resonance imaging, group-level analysis, registration, Bayesian methods, inter-individual differences, pain.

While this procedure efficiently makes the brains of all subjects overlap with regards to gross anatomical landmarks, it does not implicitly take into consideration residual differences in brain anatomy, and the location and distribution of functional regions relative to these landmarks. For example, primary visual cortex can vary in size by as much as 2-fold across different subjects' brains (Rademacher et al., 1993) and in location relative to other anatomical landmarks (Amunts et al., 2000), as can sulcal locations (Thompson et al., 1996). In some cases, inter-individual differences can be accounted for by normalization, but in other cases they cannot. For example, the cingulate sulcus is structurally dimorphic (Vogt et al., 1995)—a substantial minority of individuals possesses a double cingulate sulcus—precluding anatomical alignment using current methods. In addition, considerable variability in functional localization persists even after anatomical alignment (Duncan et al., 2009). For example, the location of visual motion-sensitive area MT can vary by more than 2 cm. The location and extent of lateral occipital cortex (Jordan et al., 2016) and fusiform face area (Allison et al., 1999; McCarthy et al., 1999) are also highly variable across individuals and located in different places relative to anatomical sulcal landmarks.

Large inter-individual differences in both brain anatomy and functional localization after anatomical alignment are a major limitation in conducting group analyses and population level inference. This is true because a large number of statistical models are performed voxel-wise (i.e., subjects are compared using a separate model at each voxel). This can lead to a situation where voxels from different functional brain regions are compared to one another in a model, significantly complicating interpretation. In addition, voxels are often used as features in prediction models, and any variation in the location of functional regions across subjects would lead to feature misalignment. Finally, it degrades the quality of the data. Though individual-subject, whole-brain fMRI data can now be collected at a resolution of 2 mm<sup>3</sup> voxels or smaller, once functional maps are combined across individuals to construct a population-level model, the effective spatial resolution is dramatically lower.

Recent approaches have sought to circumvent this problem by mapping individual brains into a functional population-level reference space rather than an anatomically based brain space. The first such model is the 'hyperalignment' procedure (Haxby et al., 2011). Here brain activity patterns corresponding to stimuli and other cognitive events are represented as vectors in a neural representational space spanned by the voxels in a local neighborhood. Hyperalignment rotates each participant's local voxel-wise activity patterns through multivariate voxel space using a Procrustes transformation to align the representational geometry across subjects. Mathematically, this is similar to Canonical Correlation Analysis (CCA). A number of refinements of hyperalignment have recently appeared, including: kernel hyperalignment (Lorbert and Ramadge, 2012), which performs nonlinear hyperalignment in an embedding space; regularized hyperalignment (Xu et al., 2012) which uses a ridge CCA formulation; the two-phase joint SVD-Hyperalignment algorithm (Chen et al., 2014), where singular value decomposition (SVD) provides a lower dimensional feature space where hyperalignment is applied; the shared response model (Chen et al., 2014) which casts the model in a probabilistic framework; and searchlight hyperalignment (Guntupalli et al., 2016) which allows for whole-brain coverage. Other methods have been developed that align subjects based on inter-subject correlations in time-series data during movie viewing. One method is functional time series alignment (Sabuncu et al., 2010), which matches voxels across subjects using a 2D 'rubber sheet' warping and maximizing inter-subject correlations across voxels (Hasson et al., 2004). Another is functional connectivity alignment (Conroy et al., 2013), which matches voxels to a functional reference by minimizing the Frobenius norm of the difference between a subject's connectivity matrix and a reference matrix with a shape-preserving penalty function. Both methods use warping and penalization strategies specific to the cortex, so it is unclear how easily they can be adapted to include subcortical regions.

This body of work shows great promise for allowing participants to vary in their functional activation patterns (Haxby et al., 2011), but suffers from several shortcomings. First, hyper-alignment requires subjects to watch a long film (up to 2 hours) to align subjects into a common representational space, and functional connectivity-based methods require substantial resting state data. Second, the choice of reference data influences which types of functional patterns can be appropriately aligned. For example, movie reference data works well for audio-visual representations but not prefrontal and limbic networks. Functional connectivity-based measures work better for limbic cortex but are expected to perform worse on object and semantic representations. Neither type of method has been tested on subcortical representations, or on clinically relevant functions such as pain and emotion. Third, these methods do not include an explicit spatial model able to make inferences on the location or extent of activation, though a few recent studies have taken steps in this direction (Nenning et al., 2017).

In this work, we focus on performing local registration of brain activation using subject-specific functional activation maps. These maps are the output of a series of voxel-wise models that quantify the activation in the BOLD signal that arises due to the stimulus of interest. We seek to warp (i.e., spatially transform) a chosen floating map (i.e., a subject-specific activation map) to some predefined reference map. In service of this goal we propose a generalized Bayes approach that is capable of cropping the subject-specific activation maps to match certain pre-defined regions of interest (ROIs). The prior distribution is estimated by matching the features of the activation maps, which are commonly defined by local peaks. The pseudo-likelihood is a representation of the similarity measure between the reference map and the warped floating map, which is given by the sum of squared difference (SSD). Furthermore, our work simultaneously models an intensity correction term which compensates for differences in the level of activation between the reference and floating maps. As the images are defined on a regular lattice, the discreteness leads to the need to utilize Gaussian process based kriging interpolation techniques (Banerjee et al., 2014; Cressie and Wikle, 2015) while realigning images.

This paper is organized as follows. Section 2 describes the data, which is from an fMRI study of thermal pain. In Section 3 we introduce our generalized Bayes framework for performing functional image registration. In Section 4 we describe a simulation study used to evaluate the performance of the method, and in Section 5 we apply the method to data from the thermal pain study. The paper concludes with a discussion.

**2. An fMRI Study of Thermal Pain .** The data are from an fMRI study of thermal pain; see Woo et al. (2015) for an in-depth discussion of the data set. In brief, 33 healthy, right-handed subjects completed the study (age  $27.9 \pm 9.0$  years, 22 females). All subjects gave informed consent, and the Columbia University Institutional Review Board approved the study.

Seven runs were administered to each subject during a single session, with each run consisting of between 58-75 trials. In our analysis the runs were concatenated and analyzed together. In each trial, thermal stimulations were delivered to the left inner forearm. Each stimulus lasted 12.5s, with 3s ramp-up and 2s ramp-down periods and 7.5s at the target temperature. In total stimuli were administered at six different temperatures, ranging from  $44.3 - 49.3^{\circ}\text{C}$  in increments of  $1^{\circ}\text{C}$ . Each stimulus was followed by a 4.5 – 8.5s pre-rating period, after which subjects rated their intensity of pain on a scale between 0 – 100. Each trial ended with a 5 – 9s resting period.

For each subject, 1845 images were acquired using a 3T Philips Achieva TX scanner at Columbia University. Structural images were acquired using high-resolution T1 spoiled gradient recall (SPGR) images. Functional echo planar images (EPIs) were acquired with

repetition time (TR) = 2000ms, echo time (TE) = 20ms, field of view = 224mm,  $64 \times 64$  matrix,  $3 \times 3 \times 3$  mm $^3$  voxels, 42 interleaved slices, parallel imaging, and sensitivity encoding (SENSE) factor 1.5. For each subject, structural images were co-registered to the mean functional image using the iterative mutual information-based algorithm in SPM8<sup>1</sup>. Thereafter, images were normalized to Montreal Neurological Institute (MNI) space using SPM8's generative segment-and-normalize algorithm. Prior to preprocessing of functional images, the first four volumes were removed to allow for image intensity stabilization. Outliers were identified using the Mahalanobis distance for the matrix of slice-wise mean and standard deviation values. The functional images were corrected for differences in slice-timing, and motion corrected using SPM8. These images were warped to SPM's normative atlas using warping parameters estimated from co-registered high-resolution structural images, and smoothed with an 8mm full width at half maximum (FWHM) Gaussian kernel. A high-pass filter of 180s was applied to the time series data.

For each subject, a voxel-wise general linear model (GLM) analysis was performed using SPM8. For each temperature, boxcar regressors convolved with the canonical hemodynamic response function (Lindquist et al., 2009), were constructed to model periods corresponding to the 12.5 s thermal stimulation and the 11 s rating periods. Other regressors of non-interest (i.e., nuisance variables) included (a) a run specific intercept; (b) linear drift across time within each run; (c) the six estimated head movement parameters (x, y, z, roll, pitch, and yaw), their mean-centered squares, their derivatives, and squared derivative for each run; (d) indicator vectors for outlier time points identified based on their multivariate distance from the other images in the sample; (e) indicator vectors for the first two images in each run; (f) signals from white matter and ventricle. For each temperature the regression coefficients corresponding to the temperature specific regressor at each voxel were combined into a single activation map. Hence, for each subject we had six different brain maps depicting the functional response across the brain to each of the temperatures.

In this work, we are primarily focused on the subject-specific mean across the six difference brain maps to analyze the inter-subject variability. We use this data to perform functional alignment. In particular, we focus our analysis on a somatosensory region of the brain; Fig 7 shows the region across subjects. Within this region one can identify several local peaks within individual participants that conform to known somatosensory areas. However, there clearly exists substantial inter-subject variability in their exact location.

**3. Methods.** The goal of image registration is to find a mapping from each voxel in one image (the floating map) to a corresponding position in another image (the reference map). This mapping involves operations on the floating map (e.g., translation, scaling, rotations) described by a transformation operator  $T$ . To formalize the problem, let  $\mathbf{Y} = (Y(s_1), Y(s_2), \dots, Y(s_V))^T$  and  $\mathbf{R} = (R(s_1), R(s_2), \dots, R(s_V))^T$  be the floating map and reference map, respectively, located at the same set of voxel locations  $\mathbf{S} = \{s_1, s_2, \dots, s_V\}$ .

A conventional approach for such a registration problem is to use a generative model of the form  $\mathbf{R} \sim_d F(\mathbf{Y}(T), \theta)$ , where  $\mathbf{Y}(T) = (Y(T(s_1)), \dots, Y(T(s_V)))^T$  and  $\mathbf{w}$  denotes all the parameters involved in the transformation operator  $T$  and distribution  $F$ . This requires the specification of a full probability distribution  $F$ . Also such a probability model will typically posit the reference map  $\mathbf{R}$  to be noisier than the floating map. For example, one can specify a generative model  $F$  as

$$(1) \quad \mathbf{R}(s) = b\mathbf{Y}(T(s, \mathbf{w})) + \mathbf{e}(s), \text{ for } s \in \mathbf{S},$$

---

<sup>1</sup>Statistical Parametric Mapping, version 8; <http://www.fil.ion.ucl.ac.uk/spm/>

where  $\mathbf{Y}(T(s, \mathbf{w}))$  is the activation of the floating map at the transformed location  $T(s, \mathbf{w})$ ,  $\mathbf{w}$  are the parameters characterizing the transformation, the factor  $b$  adjusts for the discrepancy of intensities between the floating map and reference map, and  $\mathbf{e}(s)$  is the additive noise. It is evident from (1) that  $\mathbf{R}$  is modeled as noisier than  $\mathbf{Y}$  due to the errors  $\mathbf{e}$ . This is undesirable as in practice the observed floating map is expected to be equally or more noisy than the reference, and hence generative models of this form are likely to be misspecified.

Furthermore, the generative model approach becomes problematic when working with multiple floating maps  $\mathbf{Y}_i$ , as it requires multiple generative models for the common reference map  $\mathbf{R}$ . A possible model-based solution to the multiple registration problem would be to switch the roles of  $\mathbf{Y}$  and  $\mathbf{R}$  in (1), expressing  $\mathbf{Y}(s) = b\mathbf{R}(T(s, \mathbf{w})) + \text{error}$ , which then easily extends to multiple images  $\mathbf{Y}_i$ . This formulation naturally models all the floating maps using the common reference map  $\mathbf{R}$ , and mitigates the issue of the reference map being modeled as more noisy. However, the model fit  $\hat{b}\mathbf{R}(T(s, \hat{\mathbf{w}}))$  removes all subject-specific features that are not present in the reference. Also this switched model does not offer any direct way to register the floating image to the reference. As these properties are undesirable, alternative approaches must be explored.

**3.1. Generalized Bayes framework for registration.** For the above mentioned reasons, we abandon a fully model-based formulation and instead adopt a more flexible general loss function based approach to measure and correct for relative misalignment of the individual map  $\mathbf{Y}$  with respect to the reference map  $\mathbf{R}$ . We consider  $\ell(\mathbf{R}, \mathbf{Y}(T), \mathbf{w})$  where  $\mathbf{Y}(T) = (Y(T(s_1), \dots, Y(T(s_V))^T)$  and  $\mathbf{w}$  denotes all the parameters involved in the transformation operator  $T$  and the loss function  $\ell$ .

If  $\pi(\mathbf{w})$  denotes a prior on the parameters, then a posterior distribution given the loss function  $\ell$  will be given by

$$(2) \quad \pi(\eta \mid \text{data}) = \frac{\exp(-\ell(\mathbf{R}, \mathbf{Y}(T), \mathbf{w})) \pi(\mathbf{w})}{\int \exp(-\ell(\mathbf{R}, \mathbf{Y}(T), \mathbf{w})) \pi(\mathbf{w}) d\mathbf{w}}$$

Posteriors of the form (2) that do not rely on a probability model for the data but simply a loss function are called Gibbs posteriors or generalized posteriors and are becoming increasingly common in Bayesian inference. They feature in early works of [Vovk \(1990\)](#); [Shawe-Taylor and Williamson \(1997\)](#); [McAllester \(1999\)](#); [Walker and Hjort \(2001\)](#) and their posterior summaries are referred to as Laplace Type Estimators (LTE) in [Chernozhukov and Hong \(2003\)](#) who developed extensive theoretical results on posterior concentration, asymptotic normality and valid confidence intervals for such posteriors and estimators. [Bissiri et al. \(2016\)](#) argued that updates of the form (2) are the only coherent update of a prior belief  $\pi$  given the data and the choice of the loss function  $\ell$ .

The loss function approach is compatible with multiple registration to a common template. When working with multiple floating maps, the total loss is simply the sum of the losses for the individual maps. For example, registering  $K$  images  $\mathbf{Y}_i, i = 1, \dots, K$  to a common  $\mathbf{R}$  entails simple extension of the loss function to  $\sum_{i=1}^K \ell(\mathbf{R}, \mathbf{Y}_i(T), \mathbf{w}_i)$  where the parameters  $\mathbf{w}_i$  can be image-specific or shared across images, i.e.,  $\mathbf{w}_i = \mathbf{w}$  depending on the context.

In this manuscript, we simply define the loss function as the distance between the warped image  $\mathbf{Y}(T)$  and  $\mathbf{R}$ ,

$$(3) \quad \ell(\mathbf{R}, \mathbf{Y}, b, \phi, \mathbf{w}) = \frac{1}{\phi^2} \|\mathbf{R} - b\mathbf{Y}(T(\cdot, \mathbf{w}))\|_{L_2}^2,$$

and update prior beliefs about the parameters using this loss. While there are many potential image similarity measures ([Crum et al., 2004](#)), we use the sum-of-square differences (SSD)

as it has been demonstrated as being appropriate for single-modal brain registration (Simpson et al., 2012). However, the general framework outlined here is agnostic to the choice of loss functions, and other losses like mutual information loss (Viola and Wells, 1997; Thevenaz and Unser, 1998), correlation-based losses (Gruen and Baltsavias, 1987), can be used depending on the application.

To implement this approach, decisions need to be made regarding how spatial interpolation is performed on the discrete images to obtain  $\mathbf{Y}(T)$  used by the loss function, choices of transformation operator, reference map, prior and hyperparameters. We discuss these decisions in detail below.

**3.2. Kriging Interpolation.** It is important to note that updating the parameters via optimization, or sampling using the loss function (3), would require evaluating the warped images  $\mathbf{Y}(T)$  for a given value of the transformation parameters  $\mathbf{w}$ . As the activation maps  $\mathbf{Y}$  are only observed on a predefined set of  $V$  voxels  $\mathcal{V}$ , the warped images,  $\mathbf{Y}(T)$  at the set of locations  $T(\mathcal{V})$ , are acquired through spatial interpolation. Kriging is a geostatistical smoothing and interpolation method that predict the unobserved values of the outcome at new locations given observations at current locations (Matheron, 1963; Banerjee et al., 2014; Cressie and Wikle, 2015).

To apply Kriging as an exact interpolator,  $\mathbf{Y}$  is assumed to be realization of a Gaussian process with mean  $\mu$  and spatial covariance  $\mathbf{C}$ , where  $\mathbf{C} \in \mathbb{R}^{V \times V}$  with  $C_{l,m} = \sigma^2 \exp\{-\rho\|s_l - s_m\|\}$ . Note that we do not introduce a nugget effect term in the covariance function as the purpose here is exact interpolation. The spatial parameters  $\sigma$  and  $\rho$  can be estimated within the Bayesian framework jointly with the other parameters, although increasingly, apriori estimation of these parameters is being adopted as a pragmatic strategy (Finley et al., 2019). Here we estimate them based on the marginal likelihood of  $\mathbf{Y}$  using maximum likelihood estimation.

The ordinary kriging interpolator is the best linear unbiased predictor (BLUP) under the squared error loss and can be expressed as the conditional mean of warped images given the original images, taking the form

$$(4) \quad \widehat{\mathbf{Y}(T)} = E(\mathbf{Y}(T)|\mathbf{Y}) = \frac{\mathbf{1}^T \mathbf{C}^{-1} \mathbf{Y}}{\mathbf{1}^T \mathbf{C}^{-1} \mathbf{1}} \mathbf{1} + \mathbf{K}^T \mathbf{C}^{-1} \left( \mathbf{Y} - \frac{\mathbf{1}^T \mathbf{C}^{-1} \mathbf{Y}}{\mathbf{1}^T \mathbf{C}^{-1} \mathbf{1}} \mathbf{1} \right),$$

where  $\mathbf{K} = Cov(\mathbf{Y}, \mathbf{Y}(T))$  is the covariance matrix between  $\mathbf{Y}(T)$  and  $\mathbf{Y}$  with  $K_{i,j} = \sigma^2 \exp\{-\rho\|s_i - T(s_j)\|\}$ , the covariance function evaluated at the original voxels and the warped voxels, and  $\mathbf{1}$  is a vector of ones of length  $V$ .

**3.3. Transformation Operator.** We here choose the similarity transformation (Cederberg, 2001), which consists of translation, scaling and rotation. For the case of 2D images this can be expressed as follows:

$$(5) \quad T(\mathbf{s}) = \mathbf{A}\mathbf{s} + \theta, \text{ where } \mathbf{A} = \begin{pmatrix} \cos(\omega) & -\sin(\omega) \\ \sin(\omega) & \cos(\omega) \end{pmatrix} \times \begin{pmatrix} \sigma_x & 0 \\ 0 & \sigma_y \end{pmatrix},$$

where  $\mathbf{s} = (s_x, s_y)^T$ ,  $\theta = (\theta_x, \theta_y)^T \in \mathbb{R}^2$ ,  $\omega \in (-\frac{\pi}{2}, \frac{\pi}{2})$ ,  $\sigma_x > 0$ ,  $\sigma_y > 0$ . The similarity transformation in (5) is a special case of the general 2D affine transformation. To see this, we decompose the transformation matrix  $\mathbf{A}$  as

$$(6) \quad \begin{aligned} \mathbf{A} &= \begin{pmatrix} A_{11} & A_{12} \\ A_{21} & A_{22} \end{pmatrix} \\ &= \begin{pmatrix} \cos(\omega) & -\sin(\omega) \\ \sin(\omega) & \cos(\omega) \end{pmatrix} \begin{pmatrix} 1 & \frac{A_{12} \cos(\omega) + A_{22} \sin(\omega)}{A_{22} \cos(\omega) - A_{12} \sin(\omega)} \\ 0 & 1 \end{pmatrix} \begin{pmatrix} \text{sign}(A_{11}) \sqrt{A_{11}^2 + A_{21}^2} & 0 \\ 0 & A_{22} \cos(\omega) - A_{12} \sin(\omega) \end{pmatrix}, \end{aligned}$$

where  $\omega = \arctan(A_{21}/A_{11})$ . We note that the expression above is the result of the QR decomposition. The first term is the rotation matrix. It is followed by the shearing matrix. The last term is the scaling matrix. The equivalence between Eqns. (5) and (6) can now be derived by adding constraints to eliminate the shearing effect, i.e., setting  $\frac{A_{12} \cos(\omega) + A_{22} \sin(\omega)}{A_{22} \cos(\omega) - A_{12} \sin(\omega)} = 0$ , or equivalently  $A_{11}A_{12} + A_{21}A_{22} = 0$ . Under this constraint, the decomposition can be simplified as

$$(7) \quad \mathbf{A} = \begin{pmatrix} A_{11} & A_{12} \\ A_{21} & A_{22} \end{pmatrix} = \begin{pmatrix} \cos(\omega) & -\sin(\omega) \\ \sin(\omega) & \cos(\omega) \end{pmatrix} \begin{pmatrix} \text{sign}(A_{11})\sqrt{A_{11}^2 + A_{21}^2} & 0 \\ 0 & A_{22}/\cos(\omega) \end{pmatrix}.$$

Therefore, there exists a bijection mapping between  $(\sigma_x, \sigma_y, \omega)^T$  and  $\text{vec}(A)$  under the constraint that  $A_{11}A_{12} + A_{21}A_{22} = 0$ . Furthermore, if we are interested in the positive scalings,  $\sigma_x > 0$ ,  $\sigma_y > 0$ , this can be achieved by setting  $A_{11} > 0$  and  $A_{22} > 0$ . We will exploit this connection to formulate the prior for the transformation parameters in the next section.

**3.4. Regularization Prior.** There are several obstacles in optimizing for transformation parameters in the general registration problem. First, it is an inherently ill-posed problem. A classic example where two distinct registration routines might lead to the same registration result was discussed in [Fischer and Modersitzki \(2008\)](#), where they showed a subtle example that either translation or rotation can yield the same optima. Second, it is difficult to avoid unwanted local optima. Both of these difficulties can be addressed by including a regularization, or penalty, term. In this Section we adapt this idea by introducing regularization priors for our generalized Bayes framework.

The generalized (Gibbs) posterior distribution of the warping parameters has the following form

$$(8) \quad p(T, \phi, b | \mathbf{Y}, \mathbf{R}) \propto \phi^{-V} \exp \left\{ -\frac{1}{2\phi^2} \|\mathbf{R} - b\mathbf{Y}(T)\|_{L_2}^2 \right\} \pi(T, \phi, b),$$

where  $\pi(T, \phi, b)$  is the regularization prior. We specify  $\pi(T, b, \phi) = \pi(T|\phi)\pi(b|\phi)\pi(\phi)$  for choices of  $\pi(T|\phi)$  and  $\pi(b|\phi)$  which leads to the following form of the negative log-posterior,

$$(9) \quad \frac{1}{2\phi^2} \|\mathbf{R} - b\mathbf{Y}(T)\|_{L_2}^2 + \frac{\lambda_T}{\phi^2} \text{Reg}(T) + \frac{\lambda_b}{\phi^2} (\log(b) - \log(b_0))^2,$$

where the regularizer  $\text{Reg}$  can be chosen in different ways. The terms  $\lambda_b$  and  $\lambda_T$  are the tuning parameter, which control the trade-off between the fitting of the registration likelihood and the regularization priors. The factor  $(\log(b) - \log(b_0))^2$  in the regularization part regularizes the intensity-correction term, and the term  $b_0$  is one of the hyper-parameters whose choice will be described in the next Section. To gain intuition on the necessity of this term, without penalizing values of  $b$  away from some  $b_0$ , the MCMC may become stuck in loss function valleys centered around a local minima. For example, around  $b = 0$ , the loss function will be flat for all values of the transformation parameters  $w$ . The prior for  $b$  leading to (9) is given by  $\log(b)|\phi \sim N(\log(b_0), \frac{\phi^2}{\lambda_b})$ . The regularization of  $T$ ,  $\text{Reg}(T)$ , is taken to measure the distance between the coordinates transformed by the proposed  $T$  and the some initial warping map  $T_0$  defined by hyper-parameters  $A_0$  and  $\theta_0$ . Formally, the regularizer is represented in the following way,

$$(10) \quad \text{Reg}(T) = \sum_{\mathbf{s} \in \mathcal{R}} \|T(\mathbf{s}) - T_0(\mathbf{s})\|_{L_2}^2 = \sum_{\mathbf{s} \in \mathcal{R}} \|(A - A_0)\mathbf{s} + \theta - \theta_0\|_{L_2}^2.$$

The expression of the regularizer can be further simplified as:

$$\begin{aligned} \text{Reg}(T) &= \text{trace}\{[\mathbf{s}_x \ \mathbf{s}_y \ \mathbf{1}](M - M_0)(M - M_0)^T [\mathbf{s}_x \ \mathbf{s}_y \ \mathbf{1}]^T\} \\ &= \text{trace}\{(M - M_0)^T \Sigma_s (M - M_0)\}, \end{aligned}$$

where  $M = [A \ \theta]^T = \begin{pmatrix} A_{11} & A_{12} & \theta_x \\ A_{21} & A_{22} & \theta_y \end{pmatrix}^T$ ,  $M_0 = [A_0 \ \theta_0]^T$ , and  $\Sigma_s = \begin{pmatrix} \mathbf{s}_x^T \mathbf{s}_x & \mathbf{s}_x^T \mathbf{s}_y & \mathbf{s}_x^T \mathbf{1} \\ \mathbf{s}_y^T \mathbf{s}_x & \mathbf{s}_y^T \mathbf{s}_y & \mathbf{s}_y^T \mathbf{1} \\ \mathbf{1}^T \mathbf{s}_x & \mathbf{1}^T \mathbf{s}_y & \mathbf{1}^T \mathbf{1} \end{pmatrix}$ .

Hence, using the prior  $\text{vec}(M)|\phi \sim N(\text{vec}(M_0), \frac{\phi^2}{\lambda_T} \mathbf{I} \otimes \Sigma_s^{-1})$ , where  $\otimes$  denotes the Kronecker product and  $\mathbf{I} \in \mathbb{R}^{2 \times 2}$  the identity matrix, ensures that the Gibbs posterior is of the form (9). Note that,  $M$  has 6 parameters and our transformation is only defined by 5 parameters  $\omega, \sigma_x, \sigma_y, \theta_x, \theta_y$ . As discussed in section 3.3, there is a one-to-one relationship between our parametrizations and the general 2d affine transformation parametrized by  $M$  under the constraint  $A_{11}A_{12} + A_{21}A_{22} = 0$ . Hence, we only use the multivariate normal prior for the 3-dimensional subset of  $A$  along with  $\theta$  to correspond to the priors on the rotation, scaling and translation parameters. Finally, we use the standard reference prior for the scale parameter  $\phi$ , i.e.,  $\pi(\phi) \propto 1/\phi^2$ .

Combining all the pieces in the generalized Bayes framework, the Gibbs posterior distribution of the warping parameters has the following form,

$$(11) \quad p(\theta, \sigma, \omega) \propto \phi^{-V-8} \exp \left\{ -\frac{1}{2\phi^2} \|\mathbf{R} - b\mathbf{Y}(T)\|_{L_2}^2 - \frac{\lambda_b}{\phi^2} ((\log(b) - \log(b_0))^2) - \frac{\lambda_T}{\phi^2} \text{trace}\{(M - M_0)^T \Sigma_s (M - M_0)\} \right\}.$$

**3.5. Corresponding Feature-based Prior Estimation.** Informed selection of the regularization hyper-parameters  $b_0$  and  $M_0$  is critical to ensure identifiability of the registration problem. In this Section we outline an algorithm for prior (hyperparameter) estimation based on corresponding features. The loss function (3) is solely based on the intensity information of the images, and does not use the landmark information of activation maps which is an alternate branch in the image registration. The prior (hyper-parameters) of the transformation can be estimated by incorporating information about the landmarks. This approach does not encounter computational burden with a moderate number of landmarks. In this work, we define the landmarks as the regional peaks (maxima) in clusters consisting of eight-adjacent voxels.

Let  $\mathbf{p}^R = \{s_i^R \in \mathbb{R}^2 | i = 1, \dots, N_R\}$  and  $\mathbf{p}^Y = \{s_i^Y \in \mathbb{R}^2 | i = 1, \dots, N_Y\}$  be the landmarks of reference map and the floating map, respectively.  $N_R$  and  $N_Y$  are the number of landmarks in the reference map and floating map, respectively. As a first step, the coarse sub-region of interest of the reference map is determined manually based on scientific beliefs. This sub-region contains a subset of landmarks,  $\hat{\mathbf{p}}^R \in \mathbf{p}^R$ , of size denoted by  $\hat{N}_R$ . We aim to find the corresponding subset of the landmarks  $\hat{\mathbf{p}}^Y$  from  $\mathbf{p}^Y$ . Many conventional methods, including Geometric Hashing (Mian et al., 2006) and Iterative Closest Point (Yang and Medioni, 1992; Besl and McKay, 1992), works for point set matching. However, these methods fail to capture the intensity features of the maps. In our application, as the size of the set of landmarks are relatively small (i.e.,  $N_Y < 20$  and  $\hat{N}_R < 5$ ), it is computationally efficient to apply the Brute Force Search method that tries all possible  $\hat{N}_R$  dimensional subsets of  $\mathbf{p}^Y$  to determine the matching landmarks.

The similarity transformation can be estimated using Procrustes analysis. Here we apply a modified version of Procrustes analysis, namely ABC Procrustean Algorithm (Awange et al., 2008). This version is preferable to the ordinary Procrustes algorithm as it is capable of finding the distinct scale parameters in each axial direction as opposed to the estimation of uniform scales.

The objective function used to search for correspondence is selected as the sum of squared distance between the query landmarks and the transformed candidates. Again, we need to add

a constraint term to address the ill-posed registration problem, as discussed in the beginning of this section. Formally, the mechanism can be formulated as follows,

$$(12) \quad \|\hat{\mathbf{p}}^R - T_\alpha(\hat{\mathbf{p}}^Y)\|^2 \leq d \text{ subject to } S(\hat{\mathbf{p}}^Y - T_\alpha(\hat{\mathbf{p}}^Y)) < \alpha,$$

using the transformation operator  $T_\alpha(\mathbf{s}) = \mathbf{A}_\alpha \mathbf{s} + \theta_\alpha$ .

The fact that the activation maps are discrete realizations of continuous maps motivates the use of the distance less than the threshold  $d$ , instead of minimizing the distance between landmarks. The discreteness of a map results in the bias of the coordinates of landmarks, as the underlying location of landmarks can be anywhere within a pixel. We suggest to take  $d = \hat{N}_R$  which relaxes the landmark within a voxel. The objective function creates a set of candidates of correspondence, and we choose the optimal correspondence based on the intensity loss.

The constraint  $S$  is motivated by diffusion registration (Fischer and Modersitzki, 2003) and has been applied to affine models by Chumchob and Chen (2009). By defining a function  $D: \mathbb{R}^2 \rightarrow \mathbb{R}^2$  with  $D(\mathbf{p}) = (D_1(\mathbf{p}), D_2(\mathbf{p}))^T = \mathbf{p} - T(\mathbf{p})$ , it can be expressed as follows:

$$(13) \quad S(\mathbf{p} - T(\mathbf{p})) = \frac{1}{2} \int (|\nabla D_1(\mathbf{p})|^2 + |\nabla D_2(\mathbf{p})|^2) d\mathbf{p} = \|\mathbf{I} - \mathbf{A}\|_F^2,$$

where  $\|\cdot\|_F$  denotes the Frobenius norm,  $\mathbf{I}$  is the identity matrix,  $\mathbf{A}$  is defined in equation (5). The other application of the constraint defined in Eq. (13) is to determine the orientation of  $\hat{\mathbf{p}}^Y$ . For example, in the case of  $\hat{N}^R = 3$ ,  $\hat{\mathbf{p}}^Y = \{s_1^Y, s_2^Y, s_3^Y\}$ , there are six possible correspondences to  $\hat{\mathbf{p}}^R$ , and the transformation can be derived for each of them. The mismatched correspondence may result in excessive transformation, which can cause redundant rotation and scaling. Therefore, the one minimizing  $S(\hat{\mathbf{p}}^Y - T_\alpha(\hat{\mathbf{p}}^Y))$  is used to determine the orientation of  $\hat{\mathbf{p}}^Y$ .

The threshold  $\alpha$  in Eq. 12 is chosen automatically using the Photometric Error Criterion (PEC) (Brunet et al., 2010). For each  $\alpha$ , the optimization problem in Eq. (12) is used to determine the corresponding features as well as the associated transformation. To evaluate the hyperparameter  $\alpha$ , the criterion takes advantage of intensity information, which is defined as:

$$(14) \quad \mathcal{C}(\alpha) = \frac{1}{|\mathcal{G}|} \sum_{\mathbf{p} \in \mathcal{G}} \|\mathbf{R}(\mathbf{p}) - b\mathbf{Y}(T_\alpha(\mathbf{p}))\|^2.$$

Here  $\mathcal{G}$  is the region of interest and  $|\mathcal{G}|$  is the size of the region. The discrepancy of scale between the target map and the reference map is corrected by a scaling factor  $b$ . Note that  $b$  can be estimated as the regression coefficient of  $\mathbf{R}(\mathbf{p})$  against  $\mathbf{Y}(T_\alpha(\mathbf{p}))$  without an intercept as the criterion in Eq. (14) is denoted as the mean squared error of the regression. This estimate  $b_0$  is used as a hyper-parameter in the prior of  $b$  in Section 3.5. We may further define the robust photometric error criterion (RPEC) by making a heavy-tailed distribution assumption on the residuals, for instance, the Student T distribution with a small degree freedom. The selected  $\alpha$  minimizes the criterion in Eq. (14), and produces the feature correspondence and the estimation of transformation  $M_0$  which will be considered as the hyper-parameter in the prior for  $M$  in Section . We summarize the full steps of prior estimation in Algorithm (1).

**3.6. Choice of Reference Map.** A critical decision when performing registration is deciding on an appropriate reference map. One option is to use the group mean map across all floating maps. However, this will generally make the reference map blurry and the estimated transformation largely variant. In our application, the reference subject is chosen based on scientific knowledge. For example, researchers may choose the functional map that best represents the areas of interest to be the reference. In general, we suggest to smooth the reference

map prior to model fitting, as the raw map may contain outliers that unduly influence the fit through the introduction of local modes.

It is worth noting that instead of aligning the whole brain functional map, we instead focus on estimating the transformation with respect to local regions of interest. In this way, estimation will not be unduly influenced by other 'nuisance' regions that do not contain signal of interest. The query map cropped by a rectangle bounding box from the reference map describes the local area of interest; see Figure (1) for an example. The transformed bounding boxes crop the floating maps to match and register to the query map. As the affine transformation we focus on is linear, the variability of bounding boxes on floating maps is equivalent to the variability of registration.

**3.7. Model Fitting.** The inference on the parameters is based on the draws from the posterior distribution. We use the Markov Chain Monte Carlo (MCMC) algorithm offered in the Stan software to simulate from the posterior distributions. Stan (Carpenter et al., 2017) is implemented with the No-U-Turn sampler (NUTS) (Hoffman and Gelman, 2014). We refer readers interested in details of the algorithm to the original work. Three distinct chains are fitted and initialized at values close to the prior estimates in order to accelerate the model fitting.

The only hyper-parameters that are not determined in Section 3.5 is  $\lambda_b$  and  $\lambda_T$ , which control the amount of regularization. It is common to choose such hyperparameters using cross-validation. However the use of cross-validation embedded into MCMC runs is computationally intensive, and it requires a large amount of parallel computation to cover all possible splits of the data. Vehtari et al. (2017) proposed an approach for approximating leave-one-out cross-validation using Pareto smoothed importance sampling (PSIS-LOO) which can be easily computed. Compared to the Watanabe-Akaike information (WAIC; Watanabe (2010)), we prefer PSIS-LOO as it is more robust in the finite case with weak priors or influential observations.

Along with the PSIS, we also calculate the potential scale reduction statistic (Gelman and Rubin, 1992),  $\hat{R}$ , as a metric of sampling convergence. Starting with a relatively high value of both  $\lambda_b$  and  $\lambda_T$ , we gradually fit the model with decreasing  $\lambda$  until  $\hat{R} < 1.01$ . This step keeps the model away from unwanted local modes. For each choice of  $(\lambda_b, \lambda_T)$  we compute PSIS and select the one minimizing PSIS.

**4. Simulation.** To illustrate the validity of our method we perform a simulation study using maps synthesized from the real data. Figure 1 shows an example functional activation map. The query part of the map is manually cropped and shown within the dashed rectangle. The left panel in Figure 2 shows the query map. The floating map shown in the right panel is generated by warping the reference map with the similarity transformation (including translation, scaling and rotation). The underlying parameters are translations  $\theta = (2, -5)$ , scalings  $\sigma = (0.8, 1.2)$ , and rotation  $\omega = \pi/12$ . White noise,  $10^{-5}\epsilon$  with  $\epsilon \sim N(0, 1)$ , is subsequently added to the map. We compare the learned prior information with the posterior in Figure 3, where the region surrounded by the dashed box represents the prior information and the solid box crops the matched region transformed by the posterior parameters. The boxes are generated by transforming the border box of the reference map using the prior estimates and median of posterior samples, respectively, of the transformation parameters.

The models were fitted using a sequence of regularization parameters  $(\lambda_b, \lambda_T)$  in Eq. (11). The expected log predictive density (ELPD) was estimated on each model. Figure 4 plots the  $-2 \times$  ELPD which makes it on the deviance scale. The samples produced by the model with the lowest  $-2 \times$  ELPD were used to estimate the posterior distribution. The uncertainty of transformation can be demonstrated as posterior distribution of the translation, scaling

and rotation parameters which are shown on Figure 5 with the truth superimposed as the dashed vertical line, where we can see the posterior samples successfully recover the truth. We further ran 100 simulations with different underlying transformation. Figure 6 shows the plot of posterior means against the true transformation. We could see the method recovered the truth successfully in each case.

**5. Real Data Results.** We use the data described in Section 2 to perform functional alignment. Figure 7 shows functional activation maps of the region of interest across the 33 subjects. Note that within this region there are multiple peaks. However, there also exists substantial inter-subject variability in their exact location. For example, comparing subjects 14 and 20 suggests a potential transformation consisting of rotation and shifting. Each of these functional activation maps are processed through the adaptive thresholding introduced by [Bradley and Roth \(2007\)](#). The landmarks are then identified as the regional maxima of the neighborhood of 8 adjacent locations.

The same reference map is utilized as described in the simulation; see Figure 1. The subject specific maps are shown in Figure 8, and the estimated corresponding areas are indicated using the dashed boxes. Figure 9 shows the matching area warped by the posterior mean of transformation, along with the 95% credible region of the transformations are superimposed in the gray-shaded region. The credible region of transformation is found using the density-based clustering algorithm (DBSCAN), introduced by [Ester et al. \(1996\)](#). The DBSCAN algorithm is the unsupervised clustering algorithm that separates the clusters base on the density. We refer readers to the original works for further details. To apply DBSCAN, we specify the epsilon region with at least 5 samples and a grid search of the size of the epsilon neighborhood to assure the only cluster captures about 95% of the posterior samples. The shaded region in the figure is then obtained by warping the searching box with each posterior samples of the transformation. The inter-subject variability in registration can be visualized using the estimated credible regions. For instance, subject 25 exhibits a high degree of uncertainty, while subject 14 exhibits relatively low uncertainty.

To evaluate the performance of the functional alignment procedure, we performed a second-level (across-subjects) analysis to test for significant temperature related effects. Figure 10 shows results for both the warped and unwarped maps. Studying the voxel-wise group means and standard deviations, as well as t-statistics show increased similarity in the activation profiles across subjects. After functional alignment, three peaks corresponding to posterior insula, SII, and opercular are readily apparent. In addition, the variation is decreased and more focused on the three regions-of-interest. This indicates that while the locations of the peaks are now consistent across subjects, the inter-subject differences in intensity remain. This is important for testing for brain-behavior correlations across subjects. Finally, the t-statistic is higher, indicating increased sensitivity for group-level inference.

**6. Discussion.** In this work, we propose a framework for reducing misalignment across individuals in functional brain systems. Our approach has the ability to register local brain features, defined as local peaks in the activation maps, providing a means to align functional features prior to inter-subject statistical analysis. Our generalized Bayes framework combines intensity-based information through the loss function and the feature-based information through the prior estimation, allowing us to conduct inference of the transformation via the posterior samples. In an application to fMRI data from a study of thermal pain, we found out that the registration contributes to increased sensitivity for group-level inference.

A major limitation of our work is the choice of the reference image. We currently choose it subjectively or based on the results of a meta-analysis. Therefore, in order to apply the method researchers need to check to ensure that the chosen reference pattern is shared across

subjects. In future work, we will expand our approach to model the target image as a latent map to be estimated in a data-driven manner.

Furthermore, as our data experiment measures multiple brain maps at six different temperatures, in future work we will model the within-subject variability using the registration and explore its association with other effects such as temperature. This will allow us to explore how the spatial extent of brain activation changes as a function of stimulus intensity. This provides a means to move past simply looking at spatial intensity in a specific voxel as a measure of brain activation. Another possible extension is evaluating the multilevel variability through the inference on the within-subject and between-subject transformation.

In this paper we have presented a 2-dimensional implementation of our proposed approach. However, we note that a 3-dimensional version could be constructed in an analogous manner. We began with the 2D version for illustration purposes, as it allows us to present a simplified description of the approach. In practice when applying the proposed approach to 3D data we would recommend a 3D implementation.

Finally, in future work we will seek to explore how functional registration can help improve population-level models of the functional brain representations that can be used to predict behavior, performance, clinical status and prognosis. We hypothesize that due to functional misalignment, features used in predictive models may not be properly aligned, negatively impacting predictive accuracy. Using our approach as a preliminary feature alignment step could potentially rectify this shortcoming.

**Acknowledgments.** The work presented in this paper was supported in part by NIH grants R01 EB016061 and R01 EB026549 from the National Institute of Biomedical Imaging and Bioengineering and R01 MH116026 from the National Institute of Mental Health.

## REFERENCES

Allison, T., Puce, A., Spencer, D. D., and McCarthy, G. (1999). Electrophysiological studies of human face perception. i: Potentials generated in occipitotemporal cortex by face and non-face stimuli. *Cerebral cortex*, 9(5):415–430.

Amunts, K., Malikovic, A., Mohlberg, H., Schormann, T., and Zilles, K. (2000). Brodmann's areas 17 and 18 brought into stereotaxic space—where and how variable? *Neuroimage*, 11(1):66–84.

Awange, J. L., Bae, K. H., and Claessens, S. J. (2008). Procrustean solution of the 9-parameter transformation problem. *Earth, Planets and Space*, 60(6):529–537.

Banerjee, S., Carlin, B. P., and Gelfand, A. E. (2014). *Hierarchical Modeling and Analysis for Spatial Data, Second Edition*. CRC Press, Philadelphia, PA. ID: 1598075.

Besl, P. J. and McKay, N. D. (1992). A Method for Registration of 3-D Shapes. *IEEE Transactions on Pattern Analysis and Machine Intelligence*, 14(2):239–256.

Bissiri, P. G., Holmes, C. C., and Walker, S. G. (2016). A general framework for updating belief distributions. *Journal of the Royal Statistical Society. Series B, Statistical methodology*, 78(5):1103.

Bradley, D. and Roth, G. (2007). Adaptive Thresholding using the Integral Image. *Journal of Graphics Tools*, 12(2):13–21.

Brunet, F., Bartoli, A., Navab, N., and Malgouyres, R. (2010). Pixel-based hyperparameter selection for feature-based image registration. *VMV 2010 - Vision, Modeling and Visualization*, pages 33–40.

Carpenter, B., Lee, D., Brubaker, M. A., Riddell, A., Gelman, A., Goodrich, B., Guo, J., Hoffman, M., Betancourt, M., and Li, P. (2017). Stan: A probabilistic programming language. *Journal of Statistical Software*, 76(1):1–32.

Cederberg, J. N. (2001). *A Course in Modern Geometries*. Undergraduate Texts in Mathematics. Springer New York, New York, NY.

Chen, P. H., Guntupalli, J. S., Haxby, J. V., and Ramadge, P. J. (2014). Joint SVD-Hyperalignment for multi-subject fMRI data alignment. *IEEE International Workshop on Machine Learning for Signal Processing, MLSP*, pages 1–6.

Chernozhukov, V. and Hong, H. (2003). An mcmc approach to classical estimation. *Journal of Econometrics*, 115(2):293–346.

Chumchob, N. and Chen, K. (2009). A robust affine image registration method. *International Journal of Numerical Analysis and Modeling*, 6(2):311–334.

Conroy, B. R., Singer, B. D., Guntupalli, J. S., Ramadge, P. J., and Haxby, J. V. (2013). Inter-subject alignment of human cortical anatomy using functional connectivity. *NeuroImage*, 81:400–411.

Cressie, N. and Wikle, C. K. (2015). *Statistics for spatio-temporal data*. John Wiley & Sons.

Crum, W. R., Hartkens, T., and Hill, D. L. (2004). Non-rigid image registration: Theory and practice. *British Journal of Radiology*, 77(SPEC. ISS. 2).

Duncan, K. J., Pattamadilok, C., Knierim, I., and Devlin, J. T. (2009). Consistency and variability in functional localisers. *Neuroimage*, 46(4):1018–1026.

Ester, M., Kriegel, H.-P., Sander, J., and Xu, X. (1996). A Density-Based Algorithm for Discovering Clusters in Large Spatial Databases with Noise. *Proceedings of the 2nd International Conference on Knowledge Discovery and Data Mining*, pages 226–231.

Finley, A. O., Datta, A., Cook, B. D., Morton, D. C., Andersen, H. E., and Banerjee, S. (2019). Efficient algorithms for bayesian nearest neighbor gaussian processes. *Journal of Computational and Graphical Statistics*, 28(2):401–414.

Fischer, B. and Modersitzki, J. (2003). Curvature based image registration. *Journal of Mathematical Imaging and Vision*, 18(1):81–85.

Fischer, B. and Modersitzki, J. (2008). Ill-posed medicine - An introduction to image registration. *Inverse Problems*, 24(3):1–16.

Gelman, A. and Rubin, D. B. (1992). Inference from Iterative Simulation Using Multiple Sequences Linked references are available on JSTOR for this article : Inference from Iterative Simulation Using Multiple Sequences. *Statistical Science*, 7(4):457–472.

Gruen, A. W. and Baltsavias, E. P. (1987). High-precision image matching for digital terrain model generation. *Photogrammetria*, 42(3):97–112.

Guntupalli, J. S., Hanke, M., Halchenko, Y. O., Connolly, A. C., Ramadge, P. J., and Haxby, J. V. (2016). A Model of Representational Spaces in Human Cortex. *Cerebral Cortex*, 26(6):2919–2934.

Hasson, U., Nir, Y., Levy, I., Fuhrmann, G., and Malach, R. (2004). Intersubject Synchronization of Cortical Activity during Natural Vision. *Science*, 303(5664):1634–1640.

Haxby, J. V., Guntupalli, J. S., Connolly, A. C., Halchenko, Y. O., Conroy, B. R., Gobbini, M. I., Hanke, M., and Ramadge, P. J. (2011). A common, high-dimensional model of the representational space in human ventral temporal cortex. *Neuron*, 72(2):404–416.

Hoffman, M. D. and Gelman, A. (2014). The no-U-turn sampler: Adaptively setting path lengths in Hamiltonian Monte Carlo. *Journal of Machine Learning Research*, 15:1593–1623.

Iordan, M. C., Joulin, A., Beck, D. M., and Fei-Fei, L. (2016). Locally-optimized inter-subject alignment of functional cortical regions. *arXiv preprint arXiv:1606.02349*.

Lindquist, M. A. et al. (2008). The statistical analysis of fmri data. *Statistical science*, 23(4):439–464.

Lindquist, M. A., Loh, J. M., Atlas, L. Y., and Wager, T. D. (2009). Modeling the hemodynamic response function in fmri: efficiency, bias and mis-modeling. *Neuroimage*, 45(1):S187–S198.

Lorbert, A. and Ramadge, P. J. (2012). Kernel hyperalignment. *Advances in Neural Information Processing Systems*, 3(1):1790–1798.

Matheron, G. (1963). Principles of geostatistics. *Economic geology*, 58(8):1246–1266.

McAllester, D. A. (1999). Some pac-bayesian theorems. *Machine Learning*, 37(3):355–363.

McCarthy, G., Puce, A., Belger, A., and Allison, T. (1999). Electrophysiological studies of human face perception. ii: Response properties of face-specific potentials generated in occipitotemporal cortex. *Cerebral cortex*, 9(5):431–444.

Mian, A. S., Bennamoun, M., and Owens, R. (2006). Three-dimensional model-based object recognition and segmentation in cluttered scenes. *IEEE Transactions on Pattern Analysis and Machine Intelligence*, 28(10):1584–1601.

Nenning, K. H., Liu, H., Ghosh, S. S., Sabuncu, M. R., Schwartz, E., and Langs, G. (2017). Diffeomorphic functional brain surface alignment: Functional demons. *NeuroImage*, 156(December 2016):456–465.

Ombao, H., Lindquist, M., Thompson, W., and Aston, J. (2016). *Handbook of Neuroimaging Data Analysis*. CRC Press.

Rademacher, J., Caviness Jr, V., Steinmetz, H., and Galaburda, A. (1993). Topographical variation of the human primary cortices: implications for neuroimaging, brain mapping, and neurobiology. *Cerebral Cortex*, 3(4):313–329.

Sabuncu, M. R., Singer, B. D., Conroy, B., Bryan, R. E., Ramadge, P. J., and Haxby, J. V. (2010). Function-based intersubject alignment of human cortical anatomy. *Cerebral Cortex*, 20(1):130–140.

Shawe-Taylor, J. and Williamson, R. C. (1997). A pac analysis of a bayesian estimator. In *Proceedings of the tenth annual conference on Computational learning theory*, pages 2–9.

Simpson, I. J., Schnabel, J. A., Groves, A. R., Andersson, J. L., and Woolrich, M. W. (2012). Probabilistic inference of regularisation in non-rigid registration. *NeuroImage*, 59(3):2438–2451.

Thevenaz, P. and Unser, M. (1998). Efficient mutual information optimizer for multiresolution image registration. *IEEE International Conference on Image Processing*, 1:833–837.

Thompson, P. M., Schwartz, C., Lin, R. T., Khan, A. A., and Toga, A. W. (1996). Three-dimensional statistical analysis of sulcal variability in the human brain. *Journal of Neuroscience*, 16(13):4261–4274.

Vehtari, A., Gelman, A., and Gabry, J. (2017). Practical Bayesian model evaluation using leave-one-out cross-validation and WAIC. *Statistics and Computing*, 27(5):1413–1432.

Viola, P. and Wells, W. M. (1997). Alignment by Maximization of Mutual Information. *International Journal of Computer Vision*, 24(2):137–154.

Vogt, B. A., Nimchinsky, E. A., Vogt, L. J., and Hof, P. R. (1995). Human cingulate cortex: surface features, flat maps, and cytoarchitecture. *Journal of Comparative Neurology*, 359(3):490–506.

Vovk, V. G. (1990). Aggregating strategies. *Proc. of Computational Learning Theory*, 1990.

Walker, S. and Hjort, N. L. (2001). On bayesian consistency. *Journal of the Royal Statistical Society: Series B (Statistical Methodology)*, 63(4):811–821.

Watanabe, S. (2010). Asymptotic equivalence of Bayes cross validation and widely applicable information criterion in singular learning theory. *Journal of Machine Learning Research*, 11:3571–3594.

Woo, C.-W., Roy, M., Buhle, J. T., and Wager, T. D. (2015). Distinct brain systems mediate the effects of nociceptive input and self-regulation on pain. *PLoS Biol*, 13(1):e1002036.

Xu, H., Lorbert, A., Ramadge, P. J., Guntupalli, J. S., and Haxby, J. V. (2012). Regularized hyperalignment of multi-set fMRI data. *2012 IEEE Statistical Signal Processing Workshop, SSP 2012*, pages 229–232.

Yang, C. and Medioni, G. (1992). Object modelling by registration of multiple range images. *Image and Vision Computing*, 10(3):145–155.

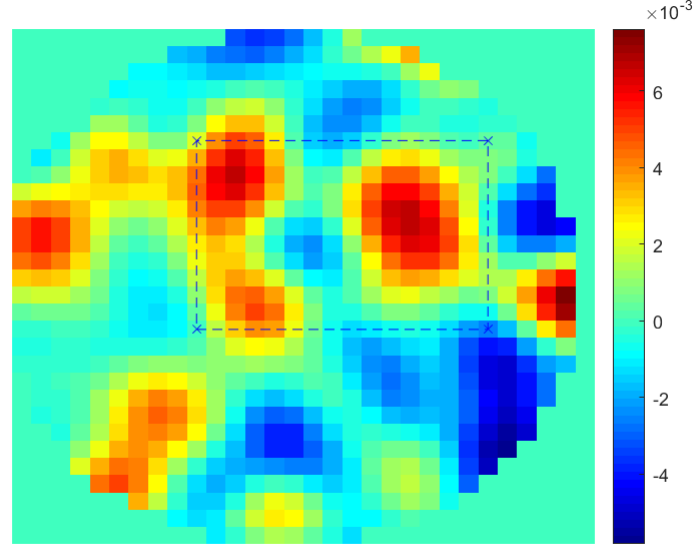


FIG 1. An example of a functional activation map. When used as a reference map, a query map indicating landmarks of interest, is manually determined and shown within the dashed rectangle.

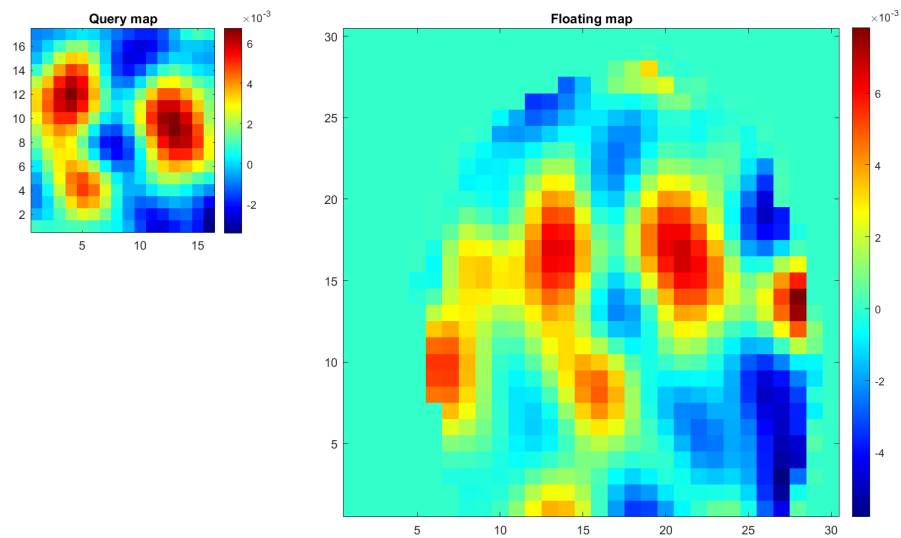


FIG 2. The query map extracted from the reference map (left column). The target map generated by warping the reference map (right column).

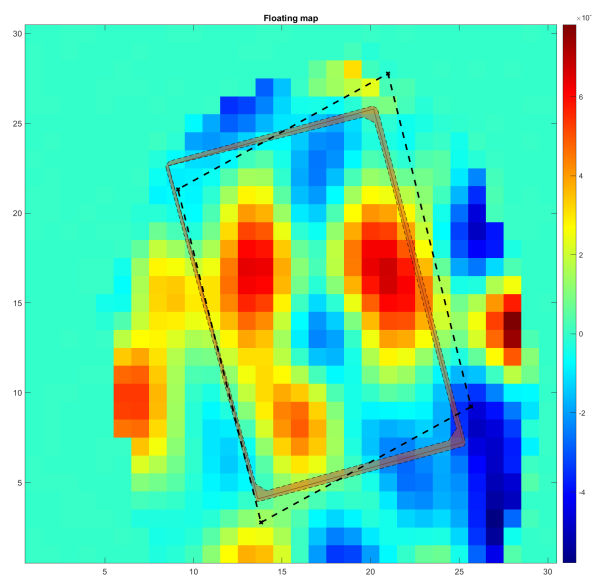


FIG 3. *Cropping box comparing the prior information (dashed box) with the posterior (solid box).*

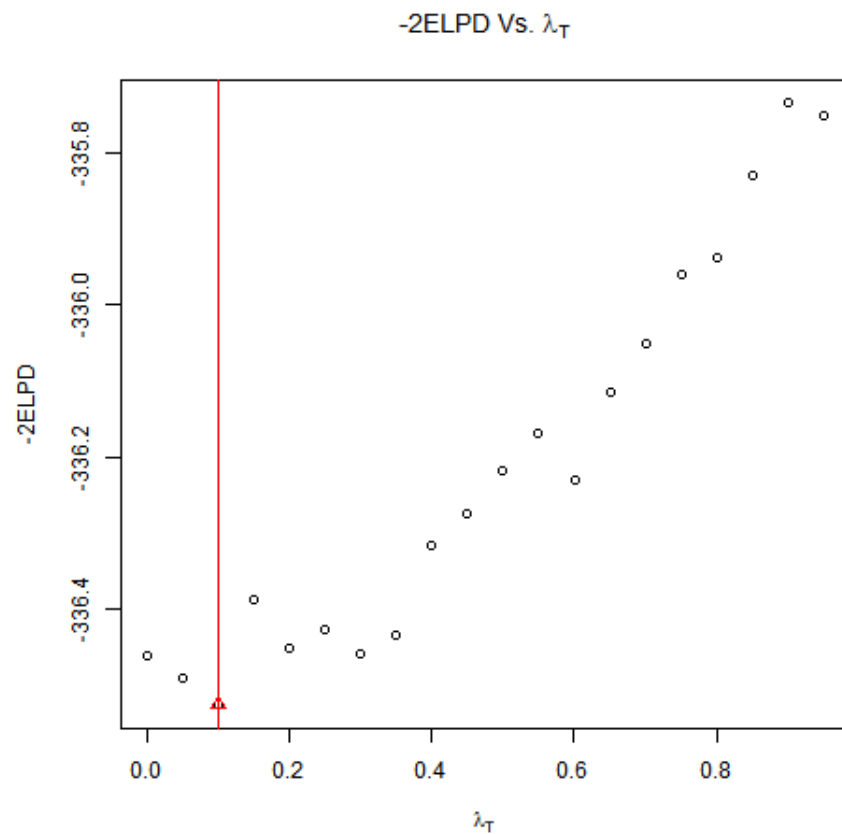


FIG 4. A plot of  $-2 \times$  expected log predictive density (ELPD) versus the regularization parameter  $\lambda_T$  given a fixed  $\lambda_b$ . The vertical bar (red) shows the selected  $\lambda_T$ , which reaches the minimum of  $-2 \times$  ELPD.

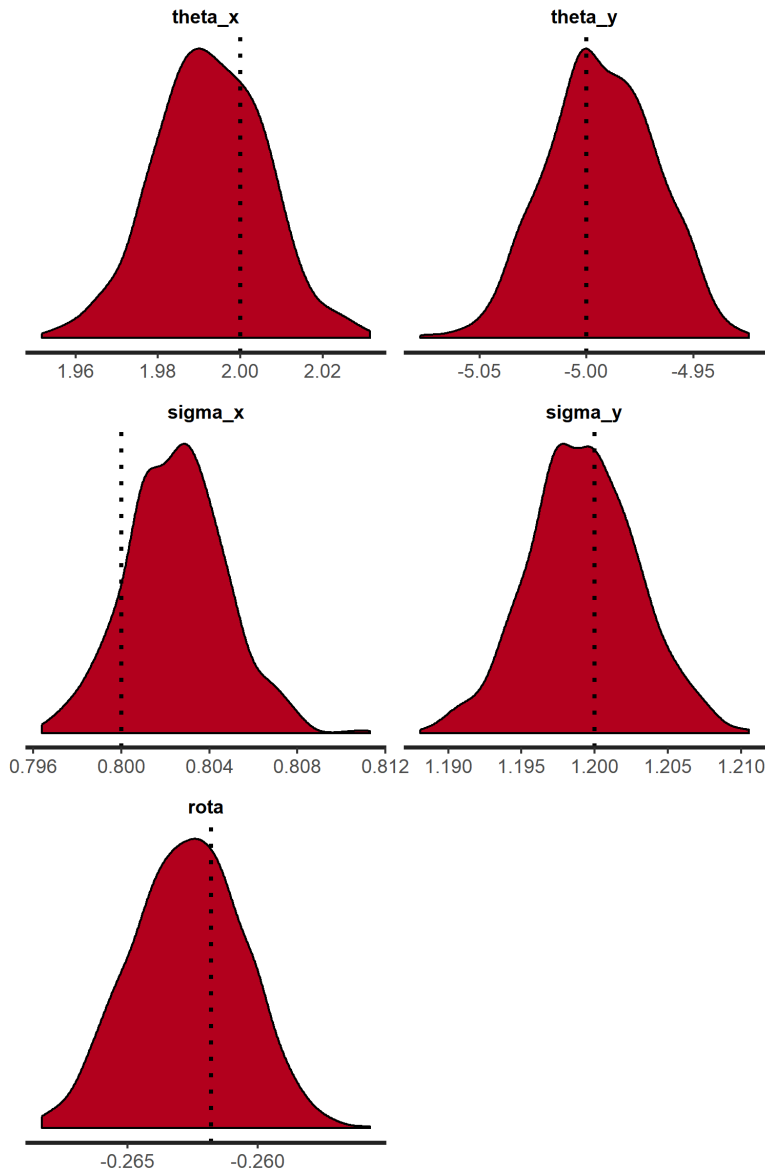


FIG 5. The estimated posterior density plot for each of the transformation parameters: translations (first row), scalings (second row), and rotations (third row). Vertical bars indicate the true parameter values.

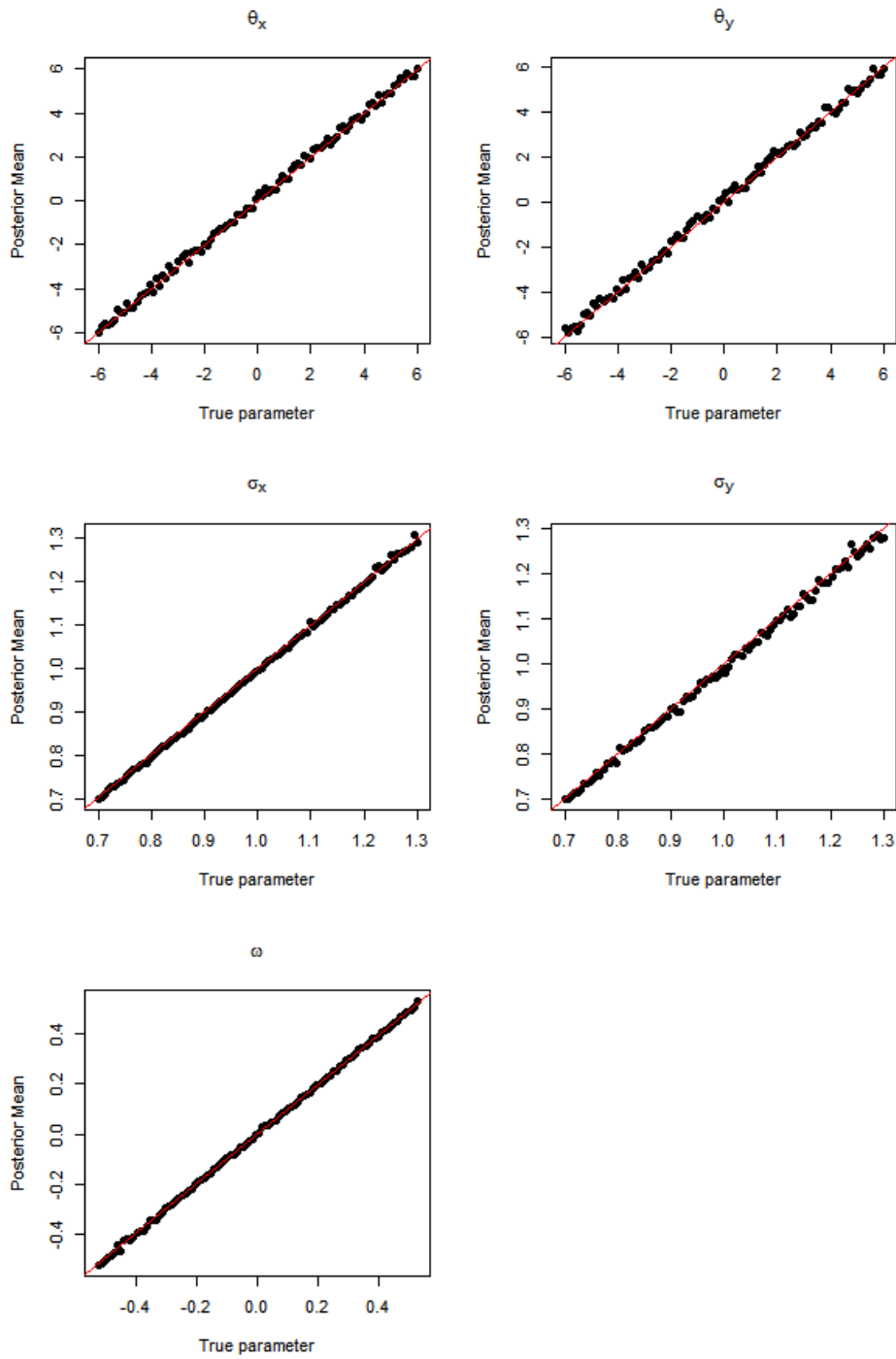


FIG 6. A plot of the posterior means against the true parameters for each transformation parameter: translations (first row), scalings (second row), and rotations (third row).

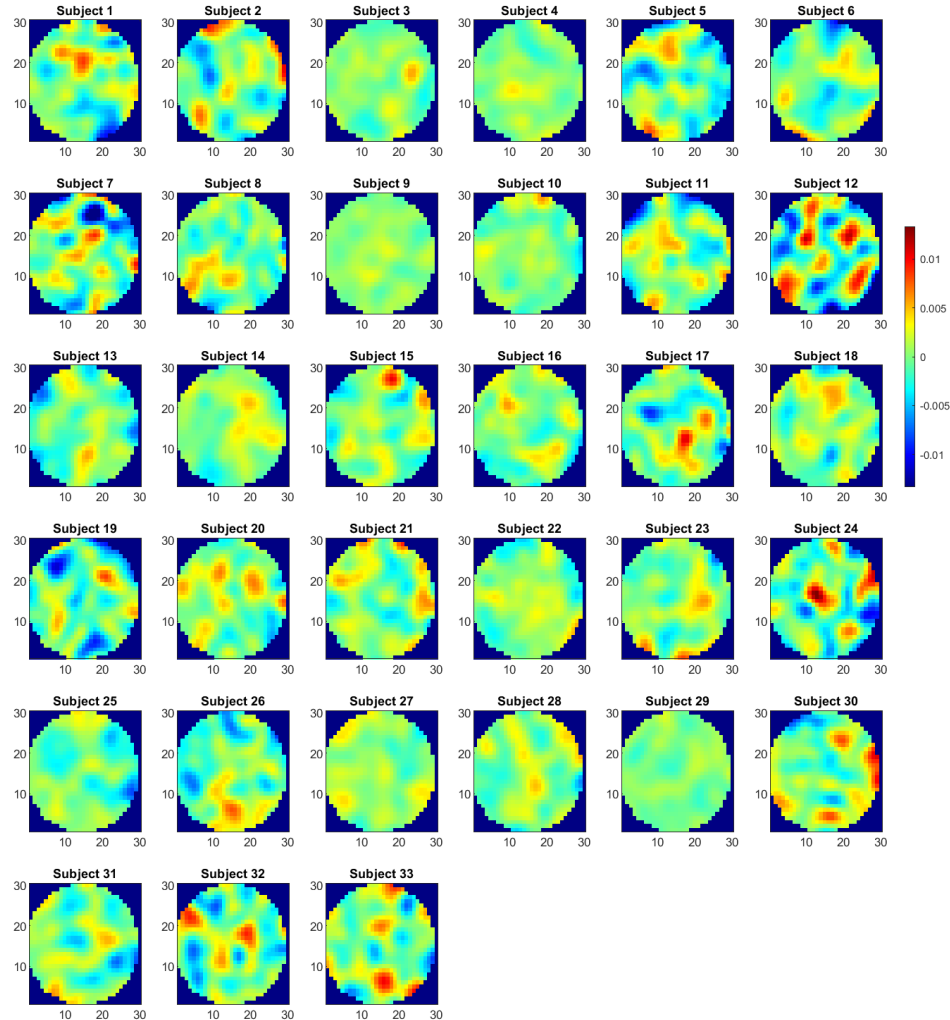


FIG 7. *Subject-specific activation maps of the region of interest across the 33 subjects. Note the differences in location of peaks across subjects, indicating significant inter-subject differences.*

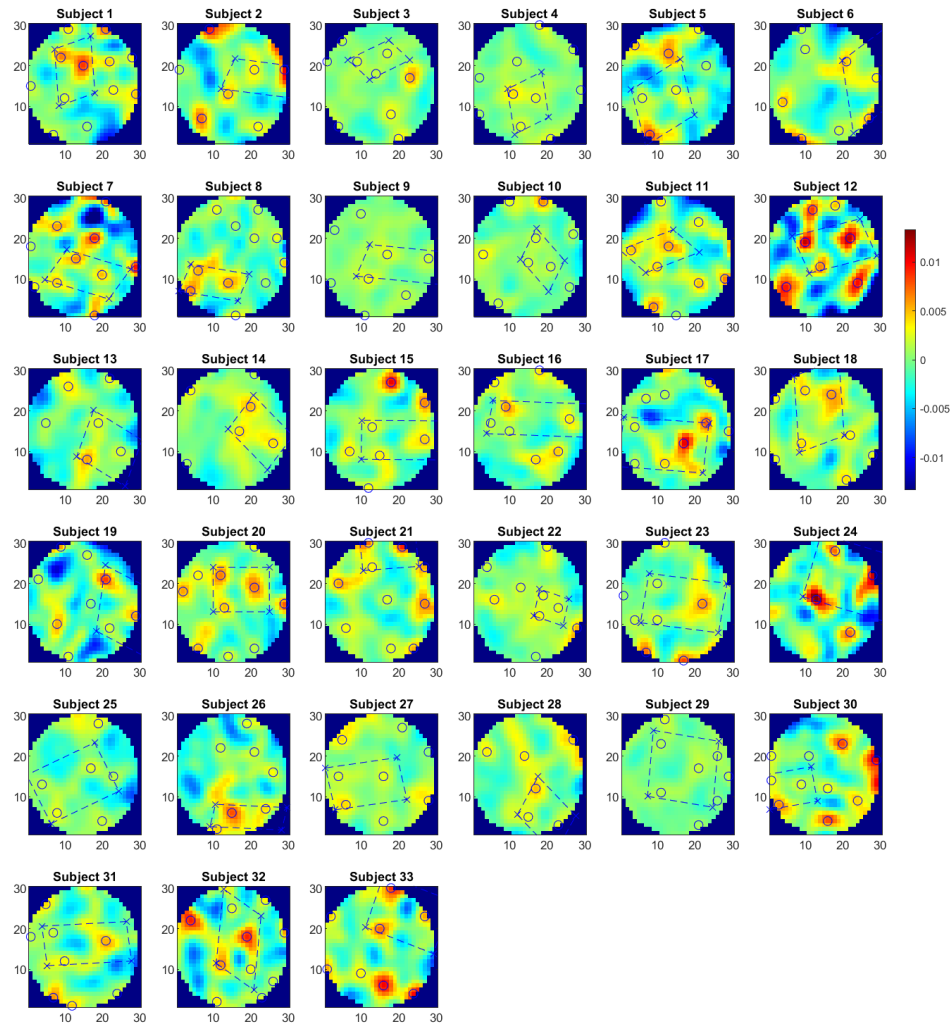


FIG 8. The corresponding cropped area (bounding box) based on prior information in each subject-specific map. The features (local peaks) are circled.

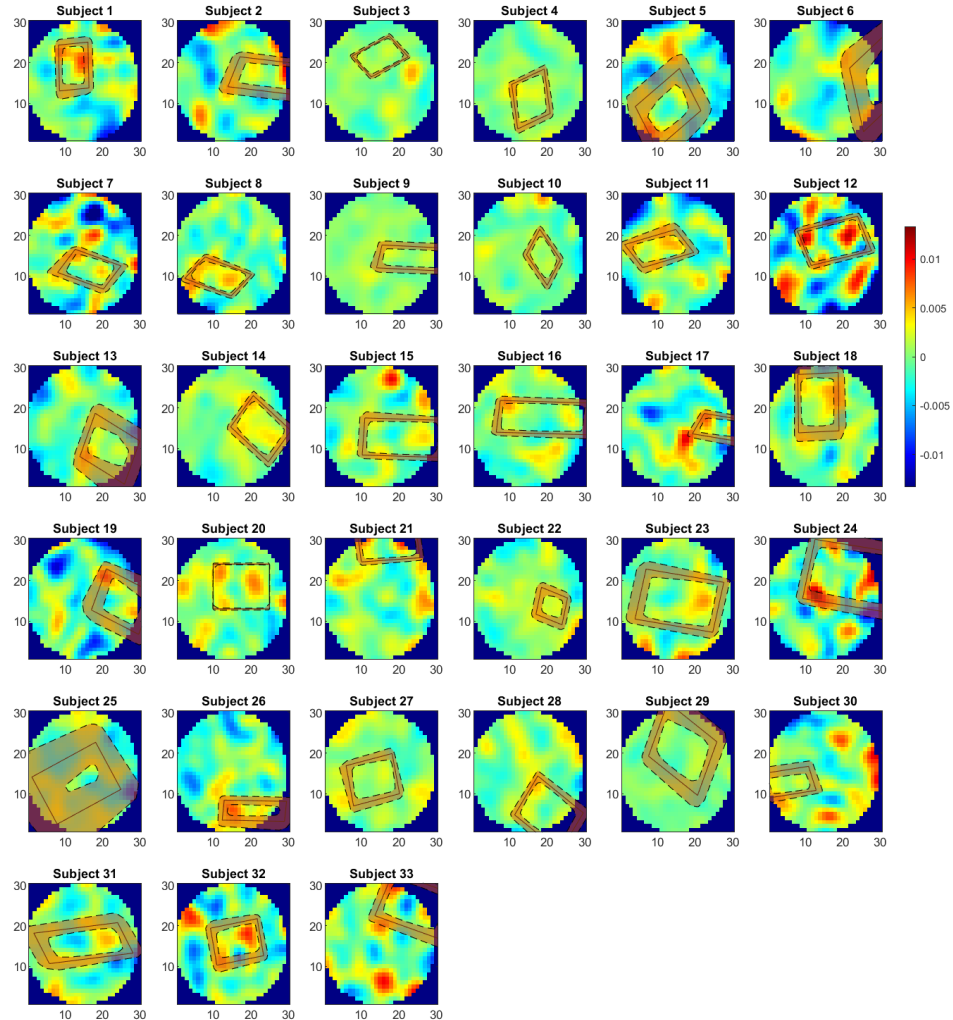


FIG 9. The warped bounding box using the transformation computed with the posterior mean is shown in solid red. The 95% credible interval of the transformation map is illustrated in the shaded area.

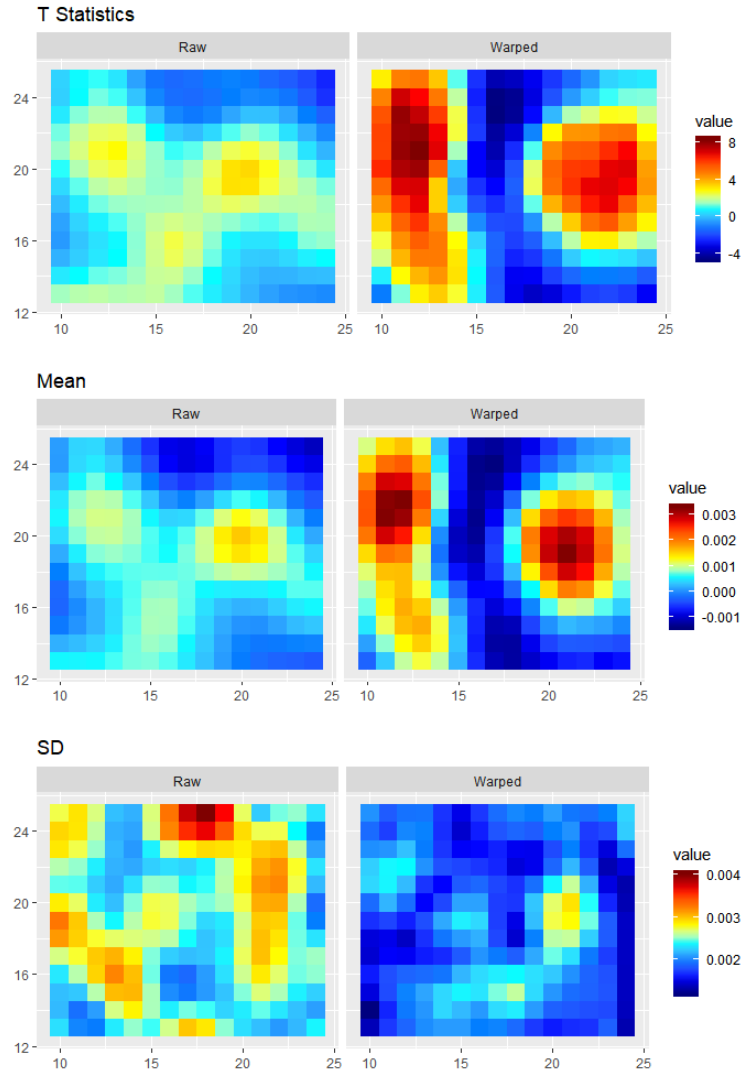


FIG 10. A comparison of the unwarped maps (left column) and warped maps (right column). Group-level statistics (T-statistics, group means, group standard deviations) are calculated for both raw maps and the warped maps.

**Algorithm 1:** Corresponding Feature-based Prior (hyper-parameter) Estimation

---

- 1 Input: reference image  $\mathbf{R}$ , reference landmarks  $\mathbf{p}^R$ , floating image  $\mathbf{Y}$ , floating landmarks  $\mathbf{p}^Y$ , bound for distance between landmarks  $d$ , bound for tuning parameter  $\alpha^{max}$ .
- 2 Construct the set  $\mathcal{S}^p = \{\hat{\mathbf{p}}^Y \in \mathbf{p}^Y : |\hat{\mathbf{p}}^Y| = |\mathbf{p}^R|\}$ ,
- 3 Construct the corresponding transformation set  $\mathcal{S}^T = \{\hat{T} : \hat{T} = \text{argmin}(\|\mathbf{p}^R - T(\hat{\mathbf{p}}^Y)\|), \text{ for } \hat{\mathbf{p}}^Y \in \mathcal{S}^p\}$ .
- 4 **for** each  $\alpha \in (0, \alpha^{max})$  **do**
- 5     Find the subset  $\hat{\mathcal{S}}_\alpha^p \subseteq \mathcal{S}^p$ , such that  $\hat{\mathcal{S}}_\alpha^p = \{\hat{\mathbf{p}}^Y \in \mathcal{S}^p : S(\hat{\mathbf{p}}^Y - T_\alpha(\hat{\mathbf{p}}^Y)) < \alpha \text{ and } \|\hat{\mathbf{p}}^R - T(\hat{\mathbf{p}}^Y)\|^2 < d\}$
- 6     Collect the corresponding transformation subset  $\hat{\mathcal{S}}_\alpha^T \subseteq \mathcal{S}^T$ ,
- 7     Compute the metric of  $\alpha$ ,  $\mathcal{C}(\alpha) = \min_{T \in \hat{\mathcal{S}}_\alpha^T} \frac{1}{|\mathcal{G}|} \sum_{\mathbf{p} \in \mathcal{G}} \|\mathbf{R}(\mathbf{p}) - b\mathbf{Y}(T(\mathbf{p}))\|^2$
- 8 Output: choose  $\alpha$  that minimizes  $\mathcal{C}(\alpha)$ . The corresponding  $T_\alpha$  is the proposed prior.

---